

IMAGING ACOUSTIC OBSTACLES BY SINGULAR AND HYPERSINGULAR POINT SOURCES

JINGZHI LI

Faculty of Science
South University of Science and Technology of China
Shenzhen, 518055, China

HONGYU LIU

Department of Mathematics and Statistics
University of North Carolina
Charlotte, NC 28223, USA

HONGPENG SUN

Institute of Mathematics
Academy of Mathematics and Systems Science, CAS
Beijing 100190, China

JUN ZOU

Department of Mathematics
The Chinese University of Hong Kong
Shatin, Hong Kong, China

(Communicated by Gunther Uhlmann)

ABSTRACT. We investigate a qualitative method for imaging acoustic obstacles in two and three dimensions by boundary measurements corresponding to hypersingular point sources. Rigorous mathematical justification of the imaging method is established, and numerical experiments are presented to illustrate the effectiveness of the proposed imaging scheme.

1. Introduction. In this paper we are concerned with the mathematical and numerical investigation of imaging acoustic obstacles in two and three dimensions by boundary measurements. This is a mathematical inverse boundary value problem associated with the Helmholtz equation. The imaging problem in two dimensions was studied in [26], where the cylindrical Bessel waves are implemented to meet the imaging purpose. The cylindrical Bessel waves are standing waves and analytic in the whole space. For the present study, we shall show that the singular point sources can also serve the imaging and reconstruction process. The point sources are spherical wave in three dimensions and the first kind Hankel function in two dimensions, which are propagating waves and one of the most common ways in emanating

2010 *Mathematics Subject Classification.* Primary: 35R30, 35J05, 78A45; Secondary: 35P25, 81U40.

Key words and phrases. Inverse acoustic scattering, boundary measurement, Dirichlet-to-Neumann map, sampling method, indicator function, hypersingular point sources.

The first author is supported by the NSF of China. (No. 91130022). The second author is supported by NSF grant, DMS 1207784. The third author is supported by the NSF of China. (No.10990012). The fourth author is substantially supported by Hong Kong RGC grants (Projects 405110 and 404611).

waves. As point sources are easily realized in acoustics and electromagnetism, and have been widely used in engineering; see, e.g. [10]. In two dimensions, we can also use more general point sources with hypersingularity. Due to the singularity (or hypersingularity) of the point sources, we need to develop essentially new techniques to show that the qualitative imaging method developed in [26] working for analytic sources remains valid for singular sources. Next, we shall briefly describe the inverse problem of our interest and the new imaging approach.

Consider an impenetrable scatterer D , which is the open complement of an unbounded domain of C^2 class in \mathbb{R}^n , $n = 2, 3$. Without loss of generality, we assume that D contains the origin. The time-harmonic acoustic wave propagation in $\mathbb{R}^n \setminus \bar{D}$ is governed by the Helmholtz equation

$$(1) \quad (\Delta + k^2)u = 0 \quad \text{in } \mathbb{R}^n \setminus \bar{D},$$

where u represents the wave pressure and $k > 0$ is the wave number. On the boundary of the obstacle ∂D , the wave exhibits various behaviors depending on the physical properties of the underlying obstacle. If D is *sound-soft*, one has $u|_{\partial D} = 0$; and if D is *sound-hard*, one has $\partial u / \partial \nu = 0$ on ∂D , where ν is the exterior unit normal to ∂D ; whereas if D is of *impedance type*, then it holds that $\partial u / \partial \nu + i\lambda u = 0$ on ∂D , where $\lambda \in C^1(\partial D)$ is a positive function. We shall write

$$(2) \quad \mathcal{B}(u) = 0 \quad \text{on } \partial D,$$

to denote either of the aforementioned three boundary conditions or a more general mixed boundary condition. We emphasize that the imaging/reconstruction method developed for the inverse problem in the present paper is independent of any such specific boundary condition, and no *a priori* knowledge of the underlying target obstacles is required during the imaging process. However, we shall stick to the sound-hard case in our subsequent discussions for the sake of exposition.

In non-invasive probings, one intends to image/identify the target obstacle D by using the knowledge of the waves away from the object. Such non-invasive techniques have been widely applied in many areas of science and technology, see, e.g., [1, 4, 5, 8, 13, 22, 23, 30] and the references therein. Many quantitative and qualitative imaging/reconstruction schemes have been developed in literature for the inverse obstacle scattering problems; see, e.g., [2, 3, 6, 7, 9, 11, 12, 14, 16, 17, 18, 19, 20, 21, 23, 24, 26, 28, 29, 30]. In [26], a new qualitative imaging method is proposed following the spirit of the linear sampling method originated in [12]. But the method makes use the near-field measurements encoded into the boundary Dirichlet-to-Neumann (DtN) or Neumann-to-Dirichlet (NtD) operator. A novel indicator function is generated which exhibits different behaviors depending on whether the sampling point is inside or outside the obstacle, thus could be used to identify the shape of the underlying obstacle. It is shown in [26] that the planar or cylindrical waves could meet the reconstruction purpose. Considering the more practical feasibility of the point sources, we will show rigorously in this work that the point sources also fulfill the imaging/reconstruction requirements well. At the same time, we extend the two-dimensional study in [26] to the three-dimensional case, as well as to the important case with partial data (see Section 3).

Now we outline the main ingredients of the new imaging scheme using the near-field data. Let $\Omega \subset \mathbb{R}^n$ be a bounded C^2 domain containing D such that $\Omega \setminus \bar{D}$ is connected. For the Helmholtz equation (1)–(2) confined over $\Omega \setminus \bar{D}$, we impose the

following boundary condition on the exterior boundary

$$(3) \quad u = f \in H^{1/2}(\partial\Omega) \quad \text{on } \partial\Omega.$$

It is assumed that 0 is not an eigenvalue to the problem (1)–(3). Hence, we have a well-defined Dirichlet-to-Neumann map Λ_D defined as

$$(4) \quad \Lambda_D(f) = \left. \frac{\partial u}{\partial \nu} \right|_{\partial\Omega},$$

where $u \in H^1(\Omega \setminus \bar{D})$ is the unique solution to (1)–(3) and ν denotes the exterior unit normal to $\partial\Omega$. It is noted that knowing Λ_D is equivalent to knowing the Cauchy data set $(u|_{\partial\Omega}, \frac{\partial u}{\partial \nu}|_{\partial\Omega})$, which encodes the near-field wave measurements. Let $\tilde{\Omega} \subset \mathbb{R}^n$ be a bounded C^2 domain such that $\Omega \Subset \tilde{\Omega}$ and $\mathbb{R}^n \setminus \tilde{\Omega}$ is connected; see Fig. 1 for the relative positions of domains D , Ω and $\tilde{\Omega}$.

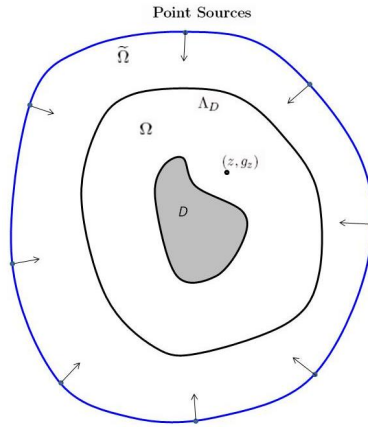


FIGURE 1. Illustration of relative positions of domains D , Ω and $\tilde{\Omega}$.

Consider the following first kind integral equation

$$(5) \quad \int_{\partial\tilde{\Omega}} (\Lambda_D - \Lambda_0)u(x; y)g(y)ds(y) = \frac{\partial G(x, z)}{\partial \nu(x)}, \quad x \in \partial\Omega, \quad z \in \Omega$$

where $u(x; y)$ is a class of point sources located at $y \in \partial\tilde{\Omega}$, Λ_0 denotes the DtN map without the inclusion D , and $G(x, y)$ is the Green’s function for the Helmholtz equation in Ω with a vanishing Dirichlet boundary value on $\partial\Omega$. The function $g(y)$ generated by (5) will play the role of an indicator in identifying ∂D in our imaging algorithm.

The method can be adjusted so that the NtD data is used. For this purpose, one imposes the following boundary condition on the exterior boundary for the Helmholtz equation (1)–(2) confined over $\Omega \setminus \bar{D}$:

$$(6) \quad \frac{\partial u}{\partial \nu} = h \in H^{-1/2}(\partial\Omega) \quad \text{on } \partial\Omega.$$

Again 0 is assumed not to be an eigenvalue to the problem (1)–(3). Then we define the NtD map Υ_D by

$$(7) \quad \Upsilon_D(h) = u|_{\partial\Omega},$$

where $u \in H^1(\Omega \setminus \bar{D})$ is the unique solution to (1), (2) and (6). The counterpart to the integral equation (5) is then given by

$$(8) \quad \int_{\partial\tilde{\Omega}} (\Upsilon_D - \Upsilon_0)u(x; y)g(y)ds(y) = G_N(x, z), \quad x \in \partial\Omega, \quad z \in \Omega,$$

where Υ_0 is the NtD map without the inclusion D . The function $G_N(x, z)$ is the Green's function for the Helmholtz equation on Ω with a vanishing Neumann boundary value on $\partial\Omega$.

The rest of the paper is organized as follows. In Section 2, we develop the imaging/reconstruction method based on the DtN map with point sources. In Section 3, we show that the imaging/reconstruction scheme developed also works by making use of partial wave emissions, and demonstrate how to modify our imaging scheme to the case with the NtD data. In Section 4, we present extensive numerical experiments to illustrate the effectiveness of the proposed method.

2. Imaging by point sources with DtN map. In this section, we develop the imaging/reconstruction scheme based on the DtN map with point sources as inputs. The discussion will be addressed for point sources in three dimensions and hypersingular ones in two dimensions. The singular source is of the form in three dimensions:

$$\frac{ik}{4\pi}h_0^{(1)}(k|x-y|) = e^{ik|x-y|}/4\pi|x-y|, \quad x \in \bar{\Omega}, \quad y \in \partial\tilde{\Omega},$$

where $h_0^{(1)}(t)$, $t \in \mathbb{R}$, is the first-kind spherical Hankel function of zeroth order, and of the following form in two dimensions:

$$w(x, y) = \frac{i}{4}H_m^{(1)}(k|x-y|)e^{im\hat{\phi}}, \quad x-y = |x-y|e^{i\hat{\phi}},$$

where $x = |x|e^{i\phi_x} \in \bar{\Omega}$ and $y = |y|e^{i\phi_y} \in \partial\tilde{\Omega}$, and $H_m^{(1)}(t)$, $t \in \mathbb{R}$, is the first-kind Hankel function of m th order.

Associated with the point-source in three dimensions, we introduce its Herglotz wave function:

$$(9) \quad (Pg)(x) := w_g(x) = \int_{\partial\tilde{\Omega}} \frac{ik}{4\pi}h_0^{(1)}(k|x-y|)g(y)ds(y), \quad x \in \bar{\Omega}, \quad y \in \partial\tilde{\Omega}$$

for $g \in L^2(\partial\tilde{\Omega})$, and define

$$(10) \quad U_{ps} := \left\{ w_g(x); w_g(x) = \int_{\partial\tilde{\Omega}} \frac{ik}{4\pi}h_0^{(1)}(k|x-y|)g(y)ds(y), \quad g(y) \in L^2(\partial\tilde{\Omega}) \right\}.$$

Similarly we introduce the following Hankel-Herglotz wave function associated with the two-dimensional hypersingular point-source:

$$(11) \quad (Hg)(x) := w_g(x) = \int_{\partial\tilde{\Omega}} \frac{i}{4}H_m^{(1)}(k|x-y|)e^{im\hat{\phi}}g(y)ds(y), \quad x \in \bar{\Omega}$$

for $g \in L^2(\partial\tilde{\Omega})$, and define

$$(12) \quad U_h := \left\{ w_g(x); w_g(x) = \int_{\partial\tilde{\Omega}} \frac{i}{4}H_m^{(1)}(k|x-y|)e^{im\hat{\phi}}g(y)ds(y), \quad g(y) \in L^2(\partial\tilde{\Omega}) \right\}.$$

Next, in light of the linear superposition for the Helmholtz system, we have the following two propositions.

Proposition 1. Let $u(x; y) \in H^1(\Omega \setminus \bar{D})$ be the solution to the Helmholtz equation (1.1)-(1.3) associated with the Dirichlet boundary value $f(x, y) = w(x, y)|_{\partial\Omega}$ with $w(x, y) = \frac{ik}{4\pi}h_0^{(1)}(k|x - y|)$ in three dimensions and $w(x, y) = \frac{i}{4}H_m^{(1)}(k|x - y|)e^{im\hat{\phi}}$ in two dimensions. Let w_g be a Herglotz wave function (point-source or Hankel resp.). Then the solution to

$$(13) \quad \begin{cases} (\Delta + k^2)u = 0 & \text{in } \Omega \setminus \bar{D} \\ u|_{\partial D} = 0, \quad u|_{\partial\Omega} = w_g|_{\partial\Omega} \end{cases}$$

is given by

$$u_g(x) = \int_{\partial\tilde{\Omega}} u(x; y)g(y)ds(y).$$

Using Proposition 1, it is straightforward to see that the solution to the following boundary value problem

$$(14) \quad \begin{cases} (\Delta + k^2)v(x; y) = 0 & \text{in } \Omega \setminus \bar{D} \\ v|_{\partial D} = -f(x, y), \quad v|_{\partial\Omega} = 0 \end{cases}$$

is given by $v(x; y) = u(x; y) - w(x, y)$.

Proposition 2. Let $v(x; y) \in H^1(\Omega \setminus \bar{D})$ be the solution to the Helmholtz equation (14) associated with the Dirichlet boundary value $f(x, y) = w(x, y)|_{\partial D}$ with $w(x, y) = \frac{ik}{4\pi}h_0^{(1)}(k|x - y|)$ in three dimensions and $w(x, y) = \frac{i}{4}H_m^{(1)}(k|x - y|)e^{im\hat{\phi}}$ in two dimensions. Let w_g be a Herglotz wave function (point-source or Hankel resp.). Then the solution to the system

$$(15) \quad \begin{cases} (\Delta + k^2)v = 0 & \text{in } \Omega \setminus \bar{D} \\ v|_{\partial D} = -w_g|_{\partial D}, \quad v|_{\partial\Omega} = 0. \end{cases}$$

can be represented by

$$v_g(x) = \int_{\partial\tilde{\Omega}} v(x; y)g(y)ds(y).$$

Since $v(x; y) = u(x; y) - w(x, y)$ in $\Omega \setminus \bar{D}$, we note the following relation for our subsequent study

$$(16) \quad \left. \frac{\partial v(x; y)}{\partial \nu(x)} \right|_{\partial\Omega} = \Lambda_D(f(x, y)|_{\partial\Omega}) - \Lambda_0(f(x, y)|_{\partial\Omega})$$

We next introduce two function spaces:

$$H_{\Delta}^1(\Omega \setminus \bar{D}) := \{u \in H^1(\Omega \setminus \bar{D}); (\Delta + k^2)u = 0 \text{ in } \Omega \setminus \bar{D} \text{ and } u|_{\partial\Omega} = 0\},$$

$$H_{\Delta}^{-1/2}(\partial\Omega) := \left\{ \frac{\partial u}{\partial \nu} \Big|_{\partial\Omega}; u \in H_{\Delta}^1(\Omega \setminus \bar{D}) \right\},$$

where the boundary values $\frac{\partial u}{\partial \nu}|_{\partial\Omega}$ and $u|_{\partial\Omega}$ are all understood in the sense of traces. Obviously, $H_{\Delta}^1(\Omega \setminus \bar{D})$ and $H_{\Delta}^{-1/2}(\partial\Omega)$ are both Banach spaces. Corresponding to these two spaces, we introduce two operators. Let $S : L^2(\partial\tilde{\Omega}) \rightarrow H_{\Delta}^1(\Omega \setminus \bar{D})$ be defined as

$$(17) \quad Sg(x) := \int_{\partial\tilde{\Omega}} v(x; y)g(y)ds(y).$$

By (15), we see $Sg(x)|_{\partial D} = -w_g(x)|_{\partial D}$ and $Sg(x)|_{\partial\Omega}=0$. Then we define $L : L^2(\partial\tilde{\Omega}) \rightarrow H_{\Delta}^{-1/2}(\partial\Omega)$ by

$$(18) \quad Lg(x) := \int_{\partial\tilde{\Omega}} \frac{\partial v(x; y)}{\partial \nu(x)} g(y) ds(y).$$

It is easily seen that $\frac{\partial Sg}{\partial \nu}(x)|_{\partial\Omega} = Lg(x)$. We are now in a position to present the crucial first kind integral equation for $g_z \in L^2(\partial\tilde{\Omega})$:

$$(19) \quad (Lg_z)(x) = \frac{\partial G(x, z)}{\partial \nu(x)}, \quad x \in \partial\Omega, \quad z \in \Omega,$$

which we know from (16) is equivalent to (cf. equation (5))

$$(20) \quad \int_{\partial\tilde{\Omega}} (\Lambda_D - \Lambda_0)(f(x, y))g_z(y) ds(y) = \frac{\partial G(x, z)}{\partial \nu(x)}, \quad x \in \partial\Omega, \quad z \in \Omega.$$

Now we give a more specific description on the Green's function $G(x, z)$ required in (19) and (20). Henceforth, we write $\Phi(x, y) = \frac{ik}{4\pi} h_0^{(1)}(k|x - y|)$ and $\Phi(x, y) = \frac{i}{4} H_0^{(1)}(k|x - y|)$ respectively as the three- and two-dimensional fundamental solutions associated with the operator $-\Delta - k^2$. We take $G(x, z) = \Phi(x, z) - p(x, z)$, where $p(x, z)$ is the (unique) solution to

$$(21) \quad (\Delta + k^2)p(x, z) = 0 \quad \text{in } \Omega; \quad p(x, z)|_{\partial\Omega} = \Phi(x, z)|_{\partial\Omega}$$

for any fixed $z \in \Omega$. It is readily seen that $G(x, z) \in H_{\Delta}^1(\Omega \setminus \bar{D})$ if $z \in D$, and this implies $\frac{\partial G(x, z)}{\partial \nu(x)}|_{\partial\Omega} \in H_{\Delta}^{-1/2}(\partial\Omega)$ if $z \in D$. For the case when the artificial domain Ω is a central disk of radius $R > 0$ in \mathbb{R}^2 , an analytic expression of $G(x, z)$ is derived in Section 4, [26]. By a similar derivation, one has that if Ω is a central ball of radius $R > 0$ in \mathbb{R}^3 ,

$$(22) \quad G(x, z) = \Phi(x, z) - \sum_{n=0}^{\infty} \sum_{m=-n}^n \frac{ik h_n^{(1)}(kR) j_n(k|z|) \overline{Y_n^m(\hat{z})}}{j_n(kR)} j_n(k|x|) Y_n^m(\hat{x}),$$

for $x = |x|\hat{x} \in \partial\Omega$ and $z = |z|\hat{z} \in \Omega$.

The function $g_z \in L^2(\partial\tilde{\Omega})$ in (19) (or equivalently in (20)) shall play the key role as an indicator function in identifying the boundary ∂D of the scatterer, depending on its different behaviors when z lies inside or outside D . We shall demonstrate the following behaviors of g_z .

Theorem 2.1. *For the solution g_z to (19) or (20), we have*

(i) *If $z \in D$, then for every $\varepsilon > 0$, there exists $g_{z,\varepsilon} \in L^2(\partial\tilde{\Omega})$ such that*

$$(23) \quad \|Lg_{z,\varepsilon}(x) - \frac{\partial G(x, z)}{\partial \nu(x)}\|_{H^{-1/2}(\partial\Omega)} \leq \varepsilon.$$

Moreover, for every $z^ \in \partial D$ and every choice of $g_{z,\varepsilon} \in L^2(\partial\tilde{\Omega})$ in (23),*

$$(24) \quad \lim_{z \rightarrow z^*} \|g_{z,\varepsilon}\|_{L^2(\partial\tilde{\Omega})} = \infty \quad \text{and} \quad \lim_{z \rightarrow z^*} \|v_{g_{z,\varepsilon}}\|_{H^1(D)} = \infty.$$

(ii) *If $z \in \Omega \setminus \bar{D}$, one can solve (19) by the Tikhonov regularization to have a regularized solution $g_{z,\varepsilon}$ in $L^2(\partial\tilde{\Omega})$, depending on a regularizer $\varepsilon > 0$. That is, $g_{z,\varepsilon}$ is the unique solution to the regularized system*

$$(25) \quad (\varepsilon I + L^*L)g = L^* \frac{\partial G(\cdot, z)}{\partial \nu}.$$

Moreover, only one of the following two possibilities occurs to the sequence $\{g_{z,\varepsilon}\}$: either there exists a sequence $\varepsilon_n \rightarrow 0^+$ such that

$$(26) \quad \lim_{\varepsilon_n \rightarrow 0^+} \|Lg_{z,\varepsilon_n}(x) - \frac{\partial G(x,z)}{\partial \nu(x)}\|_{H^{-1/2}(\partial\Omega)} = 0,$$

and

$$(27) \quad \lim_{\varepsilon_n \rightarrow 0^+} \|g_{z,\varepsilon_n}\|_{L^2(\partial\tilde{\Omega})} = \infty;$$

or, there exists a constant $C > 0$ such that for all $\varepsilon > 0$,

$$(28) \quad \|Lg_{z,\varepsilon}(x) - \frac{\partial G(x,z)}{\partial \nu(x)}\|_{H^{-1/2}(\partial\Omega)} \geq C.$$

Theorem 2.1 suggests the following procedure to determine if a point $z \in \Omega$ lies inside D or not. For two cut-off values $c_1, c_2 > 0$, one first finds a Tikhonov regularized solution $g_{z,\varepsilon}$ to (19). If $\|g_{z,\varepsilon}\|_{L^2(\partial\tilde{\Omega})} > c_1$, one counts $z \notin D$; Otherwise one can further compute the residual $Lg_{z,\varepsilon} - \partial G(\cdot, z)/\partial \nu$. If the norm of this residual is less than c_2 , one counts $z \in D$, otherwise $z \notin D$. We refer to Fig. 1 for a schematic illustration.

Numerical Reconstruction Scheme (DtN)

Select two cut-off values $c_1, c_2 > 0$.

Step 1. Collect the measurement data $\frac{\partial u(x;y)}{\partial \nu}$ on $\partial\Omega$ corresponding to the excitation $f(x, y)$ on $\partial\Omega$ for different $y \in \partial\tilde{\Omega}$.

Step 2. Select a sampling mesh \mathcal{T}_h over the domain Ω .

Step 3. For each sampling mesh point $z \in \mathcal{T}_h$, compute a Tikhonov regularized solution $g_{z,\varepsilon}$ to (19).

Step 4. If $\|g_{z,\varepsilon}\|_{L^2(\partial\tilde{\Omega})} > c_1$, we count $z \notin D$; otherwise we compute the residual $Lg_{z,\varepsilon} - \partial G(\cdot, z)/\partial \nu$. If the norm of this residual is less than c_2 , we count $z \in D$; otherwise we count $z \notin D$.

The proof of Theorem 2.1 follows a similar argument to that of Theorem 2.5 in [26], provided the following crucial results can be established in characterizing the operator L defined in (18).

Theorem 2.2. *The operator $L : L^2(\partial\tilde{\Omega}) \rightarrow H_{\Delta}^{-1/2}(\partial\Omega)$ is a linear compact operator. If k^2 is not a Dirichlet eigenvalue for $-\Delta$ in $\Omega \setminus \bar{D}$, Ω and D respectively, L is injective and has a dense range in $H_{\Delta}^{-1/2}(\partial\Omega)$.*

The proof of Theorem 2.2 relies on following results.

Lemma 2.3. *Assume that k^2 is not a Dirichlet eigenvalue for $-\Delta$ in Ω . With respect to $H^{1/2}(\partial D)$ -norm, the traces of point-source- or Hankel-Herglotz wave functions are dense in the space formed by the traces of the solutions to the Helmholtz equation on ∂D .*

Proof. Recall that $\Phi(x, y)$ is the fundamental solution associated with the operator $-\Delta - k^2$. We first show the traces of spaces U_{ps} and U_h (with $m = 0$) in (10) and (12) on $\partial\Omega$ are both dense in $H^{1/2}(\partial\Omega)$. The claims follow if we can demonstrate that any $\varphi(x) \in H^{-1/2}(\partial\Omega)$ satisfying

$$(29) \quad \int_{\partial\Omega} \int_{\partial\tilde{\Omega}} \Phi(x, y)g(y)ds(y)\overline{\varphi(x)}ds(x) = 0, \quad \forall g \in L^2(\partial\tilde{\Omega})$$

must be identically zero. By (29), along with the Fubini’s Theorem, we see

$$(30) \quad h(y) := \int_{\partial\Omega} \Phi(x, y)\overline{\varphi(x)}ds(x) = 0 \quad \text{for } y \in \partial\tilde{\Omega}.$$

By the mapping properties of the single layer potential operator (cf.[27]), we know $h(y) \in H^1_{loc}(\mathbb{R}^n \setminus \partial\Omega)$, and $h(y) = 0$ on $\partial\tilde{\Omega}$ by (30). Noting $h(y)$ is a radiating solution to the Helmholtz equation in $\mathbb{R}^n \setminus \tilde{\Omega}$, we know $h(y) = 0$ in $\mathbb{R}^n \setminus \tilde{\Omega}$ by the uniqueness of the solutions to the exterior Dirichlet problem (cf. [13]). And by further use of the unique continuation we have $h(y) = 0$ in $\mathbb{R}^n \setminus \tilde{\Omega}$. For the clarity, we denote in the sequel by γ^+ and γ^- the one-sided trace operators respectively for the disjoint domains Ω and $\mathbb{R}^n \setminus \tilde{\Omega}$. Again by the properties of the single layer potential operator, we know $\gamma^- h(y) = \gamma^+ h(y) = 0$ on $\partial\Omega$. Since $(\Delta + k^2)h(y) = 0$ in Ω , we can easily see $h(y) = 0$ also in the domain Ω by our assumption that k^2 is not a Dirichlet eigenvalue for $-\Delta$ in Ω . Now it follows readily by the jump properties of the single layer potential operator (cf. [27]) that

$$\overline{\varphi(x)} = \gamma^+ \frac{\partial h(y)}{\partial\nu} - \gamma^- \frac{\partial h(y)}{\partial\nu} = 0 \quad \text{on } \partial\Omega,$$

which proves our early claims that the restrictions of spaces U_{ps} and U_h in (10) and (12) (with $m = 0$) on $\partial\Omega$ are both dense in $H^{1/2}(\partial\Omega)$. Clearly the denseness implies that U_{ps} and U_h are dense in the space formed by all $H^1(\Omega)$ solutions to the Helmholtz equation, which in turn completes the proof of the desired result in Lemma 2.3.

It remains to consider the case with hypersingular sources in two dimensions, namely $m \geq 1$ for U_h in (12). It suffices for us to show that any $\varphi(x) \in H^{-1/2}(\partial\Omega)$ satisfying

$$(31) \quad \int_{\partial\Omega} \int_{\partial\tilde{\Omega}} \frac{i}{4} H_m^{(1)}(k|x-y|) e^{im\hat{\phi}} g(y) ds(y) \overline{\varphi(x)} ds(x) = 0, \quad \forall g \in L^2(\partial\tilde{\Omega})$$

must be identically zero. (31) is equivalent to

$$(32) \quad H(y) := \int_{\partial\Omega} \frac{i}{4} H_m^{(1)}(k|x-y|) e^{im\hat{\phi}} \overline{\varphi(x)} ds(x) = 0 \quad \forall y \in \partial\tilde{\Omega}.$$

Since $H(y)$ is a radiating solution to the Helmholtz equation in $\mathbb{R}^2 \setminus \tilde{\Omega}$, we see $H(y) = 0$ in $\mathbb{R}^2 \setminus \tilde{\Omega}$ by the uniqueness of the solutions to the exterior Dirichlet problem. Next, let $B(0, R_1)$ be a sufficiently large central ball of radius R_1 such that $\tilde{\Omega} \Subset B(0, R_1)$ and k^2 is not a Dirichlet eigenvalue for $-\Delta$ in $B(0, R_1)$. Clearly, we have $H(y) = 0$ for $y \in \mathbb{R}^2 \setminus B(0, R_1)$. Now substituting the following representation (cf. Appendix D.2, [10] or Theorem 2.12, [32])

$$(33) \quad H_m^{(1)}(k|x-y|) e^{im\hat{\phi}} = \sum_{n=-\infty}^{\infty} J_{n-m}(k|x|) e^{-i(n-m)\phi_x} H_n^{(1)}(k|y|) e^{in\phi_y}$$

for $|y| > |x|$ into (32) yields

$$(34) \quad H(y) = \sum_{n=-\infty}^{\infty} \frac{i}{4} \int_{\partial\Omega} J_{n-m}(k|x|) e^{-i(n-m)\phi_x} \overline{\varphi(x)} ds(x) H_n^{(1)}(k|R_1|) e^{in\phi_y} = 0$$

for all $y \in \partial B(0, R_1)$. Since $H_n^{(1)}(kR_1) \neq 0, \forall n \in \mathbb{Z}$, we derive from (34) that

$$(35) \quad \int_{\partial\Omega} J_n(k|x|) e^{in\phi_x} \varphi(x) ds(x) = 0, \quad \forall n \in \mathbb{Z}.$$

Using the following expansion of $H_0^{(1)}(k|x - y|)$ (cf. [10])

$$(36) \quad H_0^{(1)}(k|x - y|) = \sum_{n=-\infty}^{\infty} J_n(k|x|)H_n^{(1)}(k|y|)e^{in(\phi_y - \phi_x)} \quad \text{for } |y| > |x|,$$

and multiplying $H_n^{(1)}(k|y|)e^{in\phi_y}$ to the complex conjugate of equation (35) and then summing up for all $n \in \mathbb{Z}$, we obtain

$$h(y) = \int_{\partial\Omega} \frac{i}{4} H_0^{(1)}(k|x - y|)\overline{\varphi(x)}ds(x) = 0 \quad \forall y \in \mathbb{R}^2 \setminus \overline{B(0, R_1)}.$$

Now by a similar argument to the first part of this proof, we can show that $\varphi(x) = 0$. This completes the proof of Lemma 2.3. \square

Proof of Theorem 2.2. With the help of Lemma 2.3, the compactness and denseness of the operator L can be established by similar arguments to those for Theorem 2.3 in [26]. So we need only to show the injectivity of L . Suppose that $g \in L^2(\partial\tilde{\Omega})$ and $Lg = 0$, which imply that $Sg = 0$ and $\frac{\partial Sg}{\partial\nu} = Lg = 0$ on $\partial\Omega$. By the unique continuation, we know $Sg = 0$ in $\Omega \setminus \bar{D}$, hence $w_g = -Sg = 0$ on ∂D , which further gives $w_g(x) = 0$ in D . Then by the unique continuation again, we know $w_g = 0$ in $\tilde{\Omega}$. Next, we continue our discussions separately for the singular and hypersingular point sources.

First for the case with the singular point source $\Phi(x, y) = \frac{ik}{4\pi}h_0^{(1)}(k|x - y|)$ or $\frac{i}{4}H_0^{(1)}(k|x - y|)$, we set

$$(37) \quad T(x) = w_g(x) = \int_{\partial\tilde{\Omega}} \Phi(x, y)g(y)ds(y).$$

By the mapping property of the single layer potential operator, we know that $T(x) \in H_{loc}^1(\mathbb{R}^n \setminus \partial\tilde{\Omega})$ and is a radiating solution to the Helmholtz equation in $\mathbb{R}^n \setminus \tilde{\Omega}$. Since $\gamma^+T(x) = \gamma^-T(x) = 0$ on $\partial\tilde{\Omega}$, we know $T(x) = 0$ in $\mathbb{R}^n \setminus \tilde{\Omega}$ by the uniqueness of the exterior Dirichlet problem of the Helmholtz equation. Therefore we obtain the desired result that

$$g(x) = \gamma^+ \frac{\partial T(x)}{\partial\nu} - \gamma^- \frac{\partial T(x)}{\partial\nu} = 0 \quad \text{on } \partial\tilde{\Omega}.$$

Then for the case with the hypersingular point sources in two dimensions, we set

$$(38) \quad P(x) = w_g(x) = \int_{\partial\tilde{\Omega}} \frac{i}{4} H_m^{(1)}(k|x - y|)e^{im\phi}g(y)ds(y).$$

We can choose a central disk $B(0, R_2) \Subset \tilde{\Omega}$ of radius $R_2 > 0$ such that k^2 is not a Dirichlet eigenvalue for $-\Delta$ in $B(0, R_2)$. Plugging the expansion (33) into (38), we have

$$P(x) = \sum_{n=-\infty}^{\infty} \frac{i}{4} \int_{\partial\tilde{\Omega}} H_n^{(1)}(k|y|)e^{in\phi_y}g(y)ds(y)J_{n-m}(k|R_2|)e^{-i(n-m)\phi_x} = 0$$

for $x \in \partial B(0, R_2)$. Since $J_n(kR_2) \neq 0$ for arbitrary n , we readily know from the previous relation that

$$(39) \quad \int_{\partial\tilde{\Omega}} H_n^{(1)}(k|y|)e^{in\phi_y}g(y)ds(y) = 0, \quad \forall n \in \mathbb{Z}.$$

Now for any $x \in B(0, R_2)$, by multiplying $J_n(k|x|)e^{-in\phi_x}$ to equation (39) and then summing them over all $n \in \mathbb{Z}$ we obtain

$$(40) \quad \int_{\partial\tilde{\Omega}} \Phi(x, y)g(y)ds(y) = 0 \quad \text{for } x \in B(0, R_2),$$

where $\Phi(x, y) = i/4H_0^{(1)}(k|x-y|)$ and we have used the following expansion of $H_0^{(1)}(k|x-y|)$ (see [10])

$$H_0^{(1)}(k|x-y|) = \sum_{n=-\infty}^{\infty} J_n(k|x|)H_n^{(1)}(k|y|)e^{in(\phi_y-\phi_x)} \quad \text{for } |y| > |x|.$$

Finally, by a similar argument to that for the first case, one can verify directly that $g = 0$. This completes the proof of the injectivity of operator L , thus the proof of Theorem 2.2. \square

3. Imaging by partial wave emissions and the NtD map. In the reconstruction scheme developed in Section 2, we have basically made use of the point sources emitted from every point lying on $\partial\tilde{\Omega}$; see the schematic illustration in Fig. 1. In this section, we first show that it is sufficient for us to make use of the point sources emitted only from part of $\partial\tilde{\Omega}$. Assume that Γ is an open analytic arc in \mathbb{R}^2 or an open analytic surface in \mathbb{R}^3 , which is an open patch on the boundary $\partial\tilde{\Omega}$ of a bounded analytic domain $\tilde{\Omega} \subset \mathbb{R}^n$. Then, all our studies and the results in Section 2 still hold with $\partial\tilde{\Omega}$ replaced by Γ . Next we shall outline the major necessary modifications in the development of the imaging/reconstruction scheme using the point sources emitted only from Γ .

First of all, the indicator function $g_z \in L^2(\partial\tilde{\Omega})$ from (19) or (20) is changed naturally into the solution $g_z \in L^2(\Gamma)$ to the following first-kind integral equation

$$(41) \quad \int_{\Gamma} (\Lambda_D - \Lambda_0)(f(x, y))g_z(y)ds(y) = \frac{\partial G(x, z)}{\partial\nu(x)}, \quad x \in \partial\Omega, \quad z \in \Omega,$$

where $f(x, y)$ are the point sources as stated in Propositions 1 and 2. One can show that this modified indicator function g_z would exhibit the same behaviors as those described in Theorem 2.1 with $\partial\tilde{\Omega}$ replaced by Γ . To that end, it suffices to show that the modified operator L , namely the operator in (18) with $\partial\tilde{\Omega}$ replaced by Γ , still possesses those properties stated in Theorem 2.2. The idea for its proof would be the same as that for Theorem 2.2 in the full emissions case, with only some slight modification in proving the denseness of the modified operator L as described in the following. In fact, for the argument of the denseness of the modified operator L , following the proof of Lemma 2.3, (29) becomes

$$(42) \quad \int_{\partial\Omega} \int_{\Gamma} \Phi(x, y)g(y)ds(y)\overline{\varphi(x)}ds(x) = 0, \quad \forall g \in L^2(\Gamma),$$

which implies

$$(43) \quad h(y) := \int_{\partial\Omega} \Phi(x, y)\overline{\varphi(x)}ds(x) = 0 \quad \text{for } y \in \Gamma.$$

Since Γ is an open portion of the analytic boundary $\partial\tilde{\Omega}$, we have by the analytic continuation that $h(y) = 0$ on $\partial\tilde{\Omega}$, from which one further deduces that function φ in (42) is identically zero, thus verifying the denseness. For the two-dimensional case with hypersingular point sources, the modification is similar.

In the rest of this section, we briefly mention the necessary modifications for all of our earlier study with the DtN map to be extended to the case with NtD map. The counterpart to (20) is given by

$$(44) \quad \int_{\partial\tilde{\Omega}} (\Upsilon_D - \Upsilon_0)(f(x, y))g_z(y)ds(y) = G_N(x, z), \quad x \in \partial\Omega, \quad z \in \Omega,$$

where $f(x, y) = \partial w(x, y)/\partial\nu|_{\partial\Omega}$ with $w(x, y)$ being the point-sources as stated in Propositions 1 and 2. G_N in (44) is given by $G_N(x, z) = \Phi(x, z) - q(x, z)$, where $q(x, z)$ for any fixed $z \in \Omega$ is the (unique) solution to the system

$$(45) \quad (\Delta + k^2)q(x, z) = 0 \quad \text{in } \Omega; \quad \partial q(x, z)/\partial\nu = \partial\Phi(x, z)/\partial\nu \quad \text{on } \partial\Omega.$$

For the case when Ω is a central disk of radius $R > 0$ in \mathbb{R}^2 , an analytic expression of $G(x, z)$ is constructed (see Section 4, [26]). By a similar construction, one can show directly that if Ω is a central ball of radius $R > 0$ in \mathbb{R}^3 ,

$$(46) \quad G_N(x, z) = \Phi(x, z) - \sum_{n=0}^{\infty} \sum_{m=-n}^n \frac{ikh_n^{(1)'}(kR)j_n(k|z|\hat{z})\overline{Y_n^m(\hat{z})}}{j_n'(kR)} j_n(k|x|\hat{x})Y_n^m(\hat{x}).$$

for $x = |x|\hat{x} \in \partial\Omega$ and $z = |z|\hat{z} \in \Omega$. In the following, we set

$$(47) \quad \widehat{S}g_z(x) := \int_{\partial\tilde{\Omega}} (\Upsilon_D - \Upsilon_0)(f(x, y))g_z(y)ds(y),$$

then (44) becomes

$$(48) \quad \widehat{S}g_z(x) = G_N(x, z), \quad x \in \partial\Omega, \quad z \in \Omega.$$

Under the condition that k^2 is not a Dirichlet eigenvalue to $-\Delta$ in D and Ω , it is straightforward to modify all the corresponding arguments in Section 2 to show the following theorem on the behaviors of the solution g_z to (44) or (48).

Theorem 3.1. *For the solution g_z to (44) or (48), we have*

(i) *If $z \in D$, then for every $\varepsilon > 0$ there exists $g_{z,\varepsilon}$ to (48) such that*

$$(49) \quad \|\widehat{S}g_{z,\varepsilon}(x) - G_N(x, z)\|_{H^{1/2}(\partial\Omega)} \leq \varepsilon.$$

Moreover, for every $z^ \in \partial D$ and every choice of $g_{z,\varepsilon} \in L^2(\partial\tilde{\Omega})$ in (49),*

$$(50) \quad \lim_{z \rightarrow z^*} \|g_{z,\varepsilon}\|_{L^2(\partial\tilde{\Omega})} = \infty \quad \text{and} \quad \lim_{z \rightarrow z^*} \|v_{g_{z,\varepsilon}}\|_{H^1(D)} = \infty.$$

(ii) *If $z \in \Omega \setminus \bar{D}$, one can solve (48) by the Tikhonov regularization to have a regularized solution $g_{z,\varepsilon}$ in $L^2(\partial\tilde{\Omega})$, depending on a regularizer ε . That is, $g_{z,\varepsilon}$ is the unique solution to the system*

$$(51) \quad (\varepsilon I + \widehat{S}^* \widehat{S})g = \widehat{S}^* G_N(\cdot, z).$$

Moreover, only one of the following two possibilities occurs to the sequence $\{g_{z,\varepsilon}\}$: either there exists a sequence $\varepsilon_n \rightarrow 0^+$ such that

$$(52) \quad \lim_{\varepsilon_n \rightarrow 0^+} \|\widehat{S}g_{z,\varepsilon_n}(x) - G_N(x, z)\|_{H^{1/2}(\partial\Omega)} = 0$$

and

$$(53) \quad \lim_{\varepsilon_n \rightarrow 0^+} \|g_{z,\varepsilon_n}\|_{L^2(\partial\tilde{\Omega})} = \infty;$$

or, there exists a positive constant C such that for all $\varepsilon > 0$,

$$(54) \quad \|\widehat{S}g_{z,\varepsilon}(x) - G_N(x, z)\|_{H^{1/2}(\partial\Omega)} \geq C.$$

Based on Theorem 3.1, we can propose the following reconstruction scheme using the NtD map.

Numerical Reconstruction Scheme (NtD)

Select two cut-off values $c_1, c_2 > 0$.

Step 1. Collect the measurement data $u(x; y)$ on $\partial\Omega$ corresponding to $\partial w(x, y)/\partial\nu$ on $\partial\Omega$ for different $y \in \partial\tilde{\Omega}$.

Step 2. Select a sampling mesh \mathcal{T}_h over the domain Ω .

Step 3. For each sampling point $z \in \mathcal{T}_h$, compute a Tikhonov regularized solution $g_{z,\varepsilon}$ to the equation (48).

Step 4. If $\|g_{z,\varepsilon}\|_{L^2(\partial\tilde{\Omega})} > c_1$, we count $z \notin D$; otherwise we compute the residual $\widehat{S}g_{z,\varepsilon_n}(x) - G_N(x, z)$. If the norm of this residual is less than c_2 , we count $z \in D$; otherwise we count $z \notin D$.

Finally, we would like to mention that the previous study for the reconstruction scheme with the NtD map can be equally extended to the case with only partial wave emissions.

4. Numerical experiments and discussions. In this section, we present numerical experiments to illustrate the applicability and effectiveness of the new reconstruction scheme developed in the previous sections for the inverse obstacle scattering using near fields in two and three dimensions. Some key parameters are selected as follows: $R = 5.5$ for the radius of the surrounding disk Ω , $R_1 = 6.5$ for the radius of fictitious disk $\tilde{\Omega}$ in two dimensions (ball in three dimensions, resp.), $k = 1$ for the wave number, $m = 3$ for the order of hypersingular point sources in two dimensions, $\delta = 1\%$ for the noise level, and $c = (c_x, c_y)^T$ for the object shifting with displacements c_x and c_y from the origin in two dimensions.

In the sequel, all the synthetic near-field data of the direct problems are generated by solving the variational equation corresponding to the system (1)-(2) with isoparametric quadratic finite elements on sufficiently fine meshes and encoded as the NtD map, which measures the potential data u given the Neumann input data. The near-field data generated on the boundary $\partial\Omega$ are then subjected pointwise to the uniform random noise of the form:

$$(55) \quad U = U + \delta r_1 |U| \exp(i\pi r_2),$$

where U may be the measurement data from u or $\frac{\partial u}{\partial\nu}$, r_1 and r_2 are two uniform random numbers, both ranging from -1 to 1, and δ represents the noise level. For each mesh point z , the corresponding integral equation is discretized through the midpoint quadrature rule at the equidistantly distributed collocation points along the boundary $\partial\Omega$ in two dimensions, or transformed in the spherical coordinate system for spherical quadrature with equally spaced nodes in both latitudinal and longitudinal directions in three dimensions. The resulting linear systems are solved by using the Tikhonov regularization technique, with the corresponding regularization parameters determined by the generalized Morozov discrepancy principle.

For obstacle imaging in two dimensions, we shall test three different scatterers: a unit disk of radius 1, a kite-shaped object, which are denoted by **Di** and **K**, respectively, and a combination of **Di** and **K** (possibly at different locations). These

scatterers can be parameterized as follows:

$$(56) \quad \text{Disk:} \quad x(t) = (\cos t, \sin t), \quad 0 \leq t \leq 2\pi,$$

$$(57) \quad \text{Kite:} \quad x(t) = (\cos t + 0.65 \cos 2t - 0.65, 1.5 \sin t), \quad 0 \leq t \leq 2\pi.$$

In two dimensions, the measurement data depend on two variables: the observation location x on the medium boundary Γ and the incident direction d from the unit circle in \mathbb{R}^2 , where we write $x = (R \cos(\phi), R \sin(\phi))$ with $\phi \in [-\pi, \pi]$, and $d = (\cos(\theta), \sin(\theta))$ with $\theta \in [-\pi, \pi]$. We compute the near-field measurement data at 100 equidistantly distributed observation points $x_j = (R \cos \phi_j, R \sin \phi_j)$, $\phi_j = 2j\pi/100 - \pi$, $j = 1, 2, \dots, 100$, corresponding to 100 equidistantly distributed incident directions $d_j = (\cos \theta_j, \sin \theta_j)$, $\theta_j = 2j\pi/100 - \pi$, $j = 1, 2, \dots, 100$, around the surrounding medium circle. We may identify the observation points and incident directions with the index sequence $\{1, 2, \dots, 100\}$ and illustrate the measurement data by the contour plots of the corresponding 100×100 matrices as shown in the following examples. Hereafter, the norms of the indicator function g_z and the residual of the integral equation $\frac{\partial G(x, z)}{\partial \nu(x)} - Lg_z$ in the NtD case are denoted by g -norm and the res -norm, respectively. Furthermore, these norms are plotted by transformation via 10-based logarithm for better visualization.

Example 1. Unit disk obstacle with $c = (-1.5, -1.5)^T$.

The contour plot of the g -norm indicator function is shown in Figure 2(a), indicating a good reconstruction of the buried unit disk with the cut-off value $V_{cut} = -0.127$ as shown in Figure 2(b). For the res -norm case, the contour plot and the identified object with the cut-off value $V_{cut} = -2.03$ are shown in Figures 2(c) and (d), respectively. One observes that both indicator functions (g -norm or res -norm) work well for this example and the unknown object can soundly be detected with correct location and approximate shape and size. The blow-up behavior of the g -norm, predicted by our theoretical result, is clearly shown in Figure 2(a). The res -norm indicator function also reveals a pattern of blow-up, which has never been investigated in literature before and makes a distinct difference for the obstacle imaging between using near-field and far-field data. Unlike the usual sampling methods using far-field data (see [31] and references therein), we have now two groups of indicator functions which can be both used for numerical reconstructions.

Example 2. Kite obstacle with $c = (0, 0)^T$.

We test a non-convex kite-shaped obstacle in this example. From the contour plots of the g -norm and res -norm indicator functions, we get the reconstructed obstacle; see Figures 3(a) (with $V_{cut} = 0.159$) and (b) (with $V_{cut} = -1.91$). In particular the non-convex part is approximated very well, which shows that our reconstruction algorithm is a promising imaging scheme for even non-convex obstacles.

For this kite example, we have also tested the possibility of using partial point source emission waves for imaging purpose. The emission angle is reduced from the full range $[-\pi, \pi]$ (full circle) to $[-\pi, 0]$ (lower half circle), and then further to $[-\pi/2, 0]$ (lower right quarter circle in the fourth quadrant). For partial emission waves from lower half circle, we see in Figure 4 that the lower part of the kite is better reconstructed than its upper part, in particular in the lower left wing tip of the kite. Compared with full-range emission case, the obstacle is more deformed due to the lack of full data while the shape of the kite is still identifiable using half of the measurement data. When the emission range is further restricted on the lower right quarter circle, Figure 5 tells us that only the rough location of the

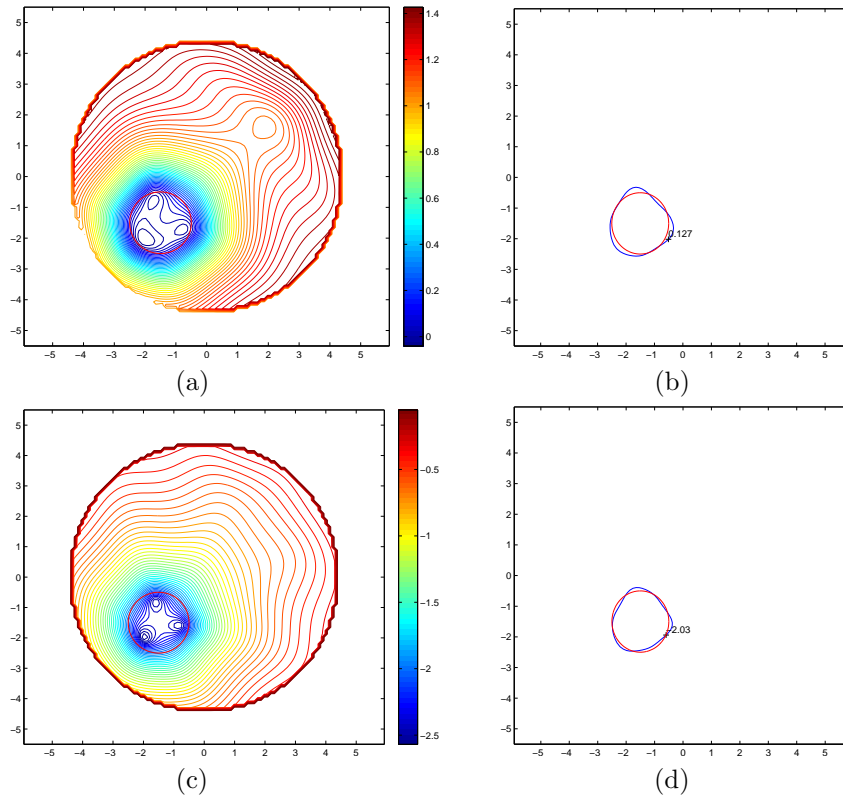


FIGURE 2. Example 1. Contour plots of the g-norm indicator (a) and res-norm indicator (c). Reconstructed obstacles from the g-norm (b) and res-norm (d) with the reference obstacle in the red line and reconstructed one in the blue line.

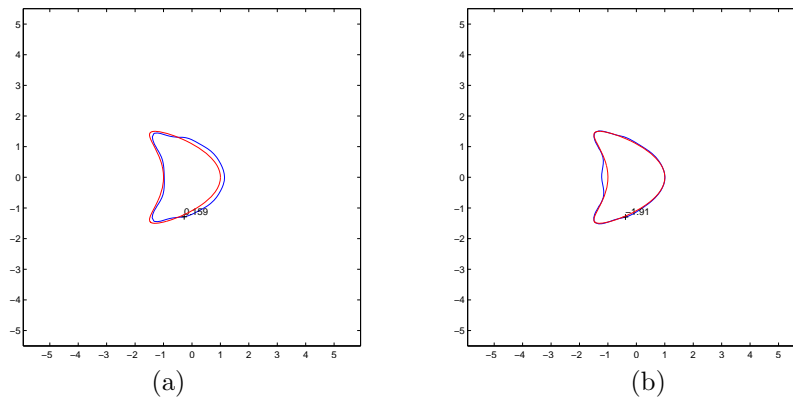


FIGURE 3. Example 2. Reconstructed obstacles from the g-norm (a) and res-norm (b) with the reference obstacle in the red line and reconstructed one in the blue line.

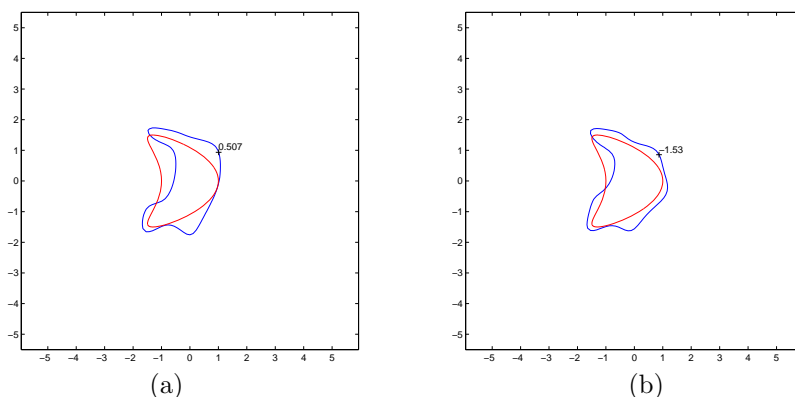


FIGURE 4. Example 2 with partial emission waves from lower half circle. Reconstructed obstacles from the g-norm (a) and res-norm (b) with the reference obstacle in the red line and reconstructed one in the blue line.

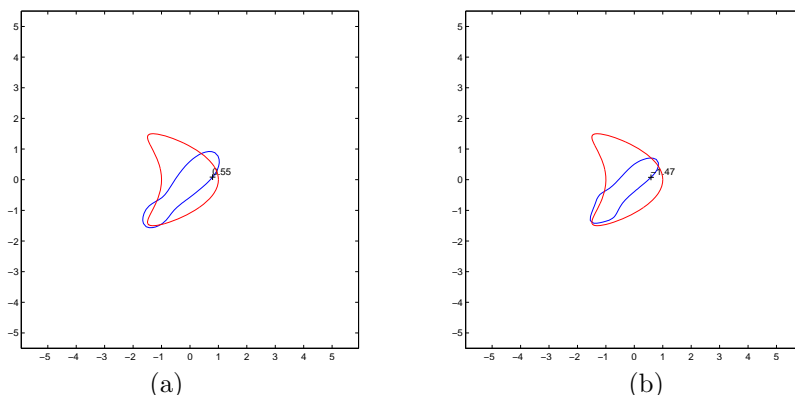


FIGURE 5. Example 2 with partial emission waves from lower left quarter circle. Reconstructed obstacles from the g-norm (a) and res-norm (b) with the reference obstacle in the red line and reconstructed one in the blue line.

kite and the lower part facing the emission angles can be reasonably approximated, and the upper left part of the kite cannot be imaged well due to the limited data and the fast decay properties of hypersingular point sources. This example verifies our claim in Section 3 and endows practitioners with the chance to obtain rough image information based on limited emission waves, for instance, in case that only location and crude shape are preferred, such as mine detection..

Example 3. A combination of disk and kite obstacles with $c_{disk} = (-2, -2)$ and $c_{kite} = (2, 2)^T$.

Based on the contour plot of the g-norm indicator function, the reconstructed obstacle components are shown in Figure 6(a) (with $V_{cut} = 0.182$); On the other hand, the reconstruction based on the contour plot of the res-norm indicator function is shown in Figure 6(b) (with $V_{cut} = -2.47$). We can see that, due to strong interaction from the close distance, those parts of different objects facing each other

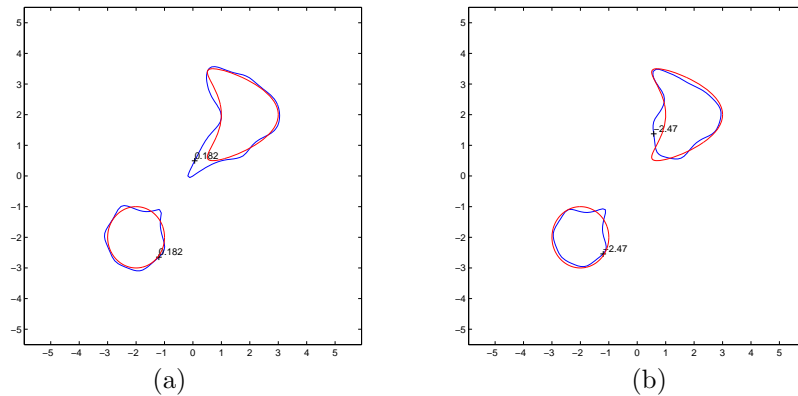


FIGURE 6. Example 3. Reconstructed obstacles from the g-norm (a) and res-norm (b) with the reference obstacle in the red line and reconstructed one in the blue line.

are attracted to a certain degree, which causes those parts looks a bit deformed. Nevertheless, the identified object is still a reasonable approximation of the original multi-component unknown obstacle. In this example, the reconstruction based on the g-norm indicator seems better than that based on the res-norm, particularly for those parts facing each other.

We emphasize that the choice of the cut-off values is crucial for the quality of the numerical reconstruction. The same strategy we proposed in [25] can be extended here for the determination of the cut-off values we need in the obstacle imaging, by taking the advantage of the mutual interaction between obstacle components. We are now using this example to illustrate the effectiveness of such choice scheme.

In fact, we may think only the kite obstacle is the unknown scatterer in this example. To reconstruct its shape, we place a reference (known) obstacle component into the physical surrounding, e.g., the unit disk in the example. Then we carry out our reconstruction algorithm, and read out the cut-off value from the isoline which matches best the reference obstacle component, namely the unit disk. Then we take this cut-off value to further recover other unknown obstacle components, e.g., the kite in this example. We see clearly that the cut-off values of the two objects are correlated with each other due to the mutual interaction of the wave between the objects. Furthermore, those parts of objects facing each other are slightly attracted due to much stronger interaction effects with smaller distance between those parts.

Finally, we test two three-dimensional examples. The scatterers are chosen to be respectively a unit ball centered at the origin and an acorn parametrized by $\rho^2(\theta) = \frac{9}{25}(\frac{17}{4} + 2\cos(3\theta))$ evolving around the z-axis [15, 13]; see Figures 7(a) and 8(a). The observed data are measured in 41×41 pairs of equally-spaced latitudinal and longitudinal coordinates on the surrounding sphere $\partial\Omega$ with point source waves emitted from 41×41 pairs of equally-spaced latitudinal and longitudinal directions.

Example 4. Unit ball obstacle centered at the origin.

The computational region is approximated by triangulation in Figures 7(b). The reconstructed obstacles are shown in Figure 7(c) based on the g-norm indicator with the cut-off value 0.142, and in Figure 7(d) based on the res-norm indicator with the cut-off value -0.8157 .

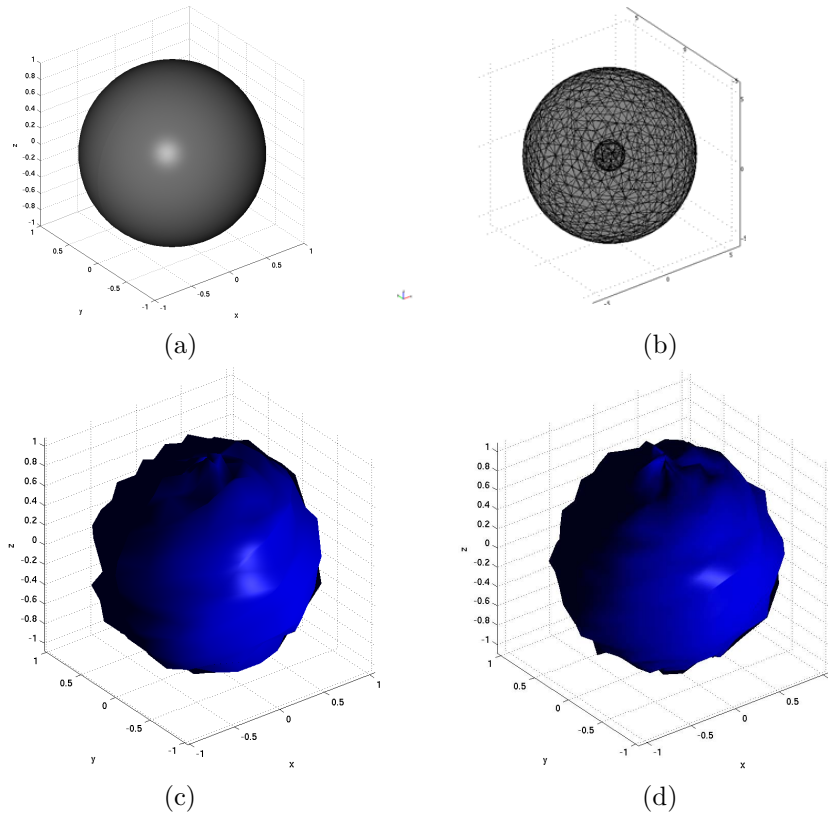


FIGURE 7. Example 4 with the singular point source. Exact shape of the unit sphere (a) and triangulation (b). Reconstructed obstacles from the g-norm (c) ($V_{cut} = 0.142$) and res-norm (d) ($V_{cut} = -0.815$), respectively.

Example 5. Acorn obstacle.

The last example is a three-dimensional nonconvex scatterer, and the computational region is approximated by triangulation in Figures 8(b). Figures 8(c) and 8(d) show the reconstructed shapes for the acorn with the g-norm and res-norm indicators, respectively, with cut-off value being 0.098 and -0.632 . The location, shape and size of the reconstructed object are all well approximated if noise is taken into account. Once again, this example demonstrate the applicability of the indicators to determine a reasonably approximated unknown obstacle for practical use in three dimensions.

Acknowledgments. We would like to thank the anonymous referee very much for the valuable comments and suggestions.

REFERENCES

- [1] H. Ammari, “An Introduction to Mathematics of Emerging Biomedical Imaging,” Mathematics and Applications, **62**, Springer-Verlag, Berlin, 2008.
- [2] H. Ammari, J. Garnier, H. Kang, M. Lim and K. Solna, *Multistatic imaging of extended targets*, SIAM J. Imaging Sci., **5** (2012), 564–600.

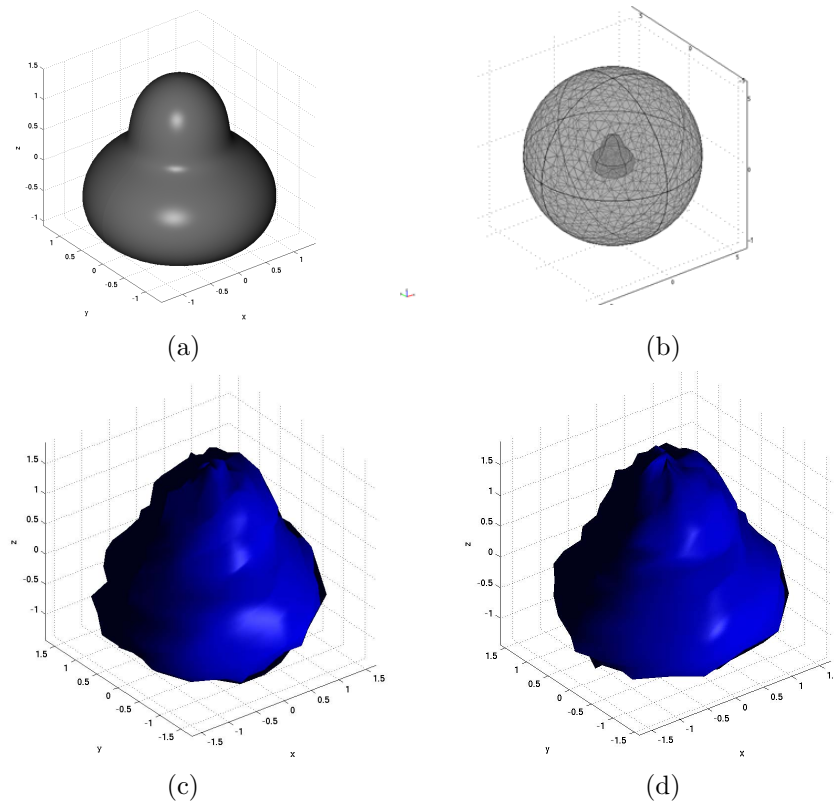


FIGURE 8. Example 5 with the singular point source. Exact shape of the acorn (a) and triangulation (b). Reconstructed obstacles from the g-norm (c) ($V_{cut} = 0.098$) and res-norm (d) ($V_{cut} = -0.632$), respectively.

- [3] H. Ammari, R. Griesmaier and M. Hanke, *Identification of small inhomogeneities: Asymptotic factorization*, Math. Comp., **76** (2007), 1425–1448.
- [4] H. Ammari and H. Kang, “Expansion Methods,” Handbook of Mathematical Methods in Imaging, Springer-Verlag, New York, 2011, 447–499.
- [5] H. Ammari and H. Kang, “Reconstruction of Small Inhomogeneities from Boundary Measurements,” Springer-Verlag, Berlin Heidelberg, 2004.
- [6] H. Ammari, H. Kang, H. Lee and W. K. Park, *Asymptotic imaging of perfectly conducting cracks*, SIAM J. Sci. Comput., **32** (2010), 894–922.
- [7] T. Arens, *Why the linear sampling method works*, Inverse Problems, **20** (2004), 163–173.
- [8] F. Cakoni and D. Colton, “Qualitative Methods in Inverse Scattering Theory,” Springer-Verlag, Berlin Heidelberg, 2006.
- [9] M. Cheney, *The linear sampling method and the MUSIC algorithm*, Inverse Problems, **17** (2001), 591–595.
- [10] W. C. Chew, “Waves and Fields In Inhomogeneous Media,” Van Nostrand Reinhold, 1990.
- [11] D. Colton, H. Haddar and M. Piana, *The linear sampling method in inverse electromagnetic inverse scattering theory*, Inverse Problems, **19** (2003), S105–S137.
- [12] D. Colton and A. Kirsch, *A simple method for solving inverse scattering problems in the resonance region*, Inverse Problems, **12** (1996), 383–393.
- [13] D. Colton and R. Kress, “Inverse Acoustic and Electromagnetic Scattering Theory,” 2nd edition, Springer-Verlag, New York, 1998.

- [14] D. Colton and R. Kress, *Using fundamental solutions in inverse scattering*, Inverse Problems, **22** (2006), R49–r66.
- [15] D. Colton and P. Monk, *The numerical solution of the three-dimensional inverse scattering problem for time harmonic acoustic waves*, SIAM J. Sci. Stat. Comput., **8** (1987), 278–291.
- [16] D. Colton and P. Monk, *A linear sampling method for the detection of leukemia using microwaves*, SIAM J. Appl. Math., **58** (1998), 926–941.
- [17] B. Gebauer, M. Hanke, A. Kirsch, W. Muniz and C. Schneider, *A sampling method for detecting buried objects using electromagnetic scattering*, Inverse Problems, **21** (2005), 2035–2050.
- [18] T. Ide, H. Isozaki, S. Nakata, S. Siltanen and G. Uhlmann, *Probing for electrical inclusions with complex spherical waves*, Commu. Pure. Appl. Math., **60** (2007), 1415–1442.
- [19] M. Ikehata and H. Itou, *Extracting the support function of a cavity in an isotropic elastic body from a single set of boundary data*, Inverse Problems, **25** (2009), 105005.
- [20] M. Ikehata, *Enclosing a polygonal cavity in a two-dimensional bounded domain from Cauchy data*, Inverse Problems, **15** (1999), 1231–1241.
- [21] M. Ikehata, *How to draw a picture of an unknown inclusion from boundary measurements. Two mathematical inversion algorithms*, J. Inv. Ill-posed Problems, **7** (1999), 255–271.
- [22] V. Isakov, “Inverse Problems for Partial Differential Equations,” 2nd edition, Springer-Verlag, New York, 2006.
- [23] A. Kirsch and N. Grinberg, “The Factorization Method for Inverse Problems,” Oxford University Press, 2008.
- [24] J. Z. Li, H. Y. Liu and J. Zou, *Multilevel linear sampling method for inverse scattering problems*, SIAM J. Sci. Comp., **30** (2008), 1228–1250.
- [25] J. Z. Li, H. Y. Liu and J. Zou, *Strengthened linear sampling method with a reference ball*, SIAM J. Sci. Comp., **31** (2009), 4013–4040.
- [26] J. Z. Li, H. Y. Liu, H. P. Sun and J. Zou, *Reconstructing acoustic obstacle by planar and cylindrical waves*, J. Math. Phys., **53** (2012), 103705 .
- [27] W. Mclean, “Strongly Elliptic Systems and Boundary Integral Equations,” Cambridge University Press, 2000.
- [28] G. Nakamura and K. Yoshida, *Identification of a non-convex obstacle for acoustical scattering*, J. Inv. Ill-posed Problems, **15** (2007), 611–624.
- [29] R. Potthast, *A fast new method to solve inverse scattering problem*, Inverse Problem, **12** (1996), 731–742.
- [30] R. Potthast, “Point Sources and Multipoles in Inverse Scattering Theory,” Chapman& Hall/CRC Research Notes in Math., 2001.
- [31] R. Potthast, *A survey on sampling and probe methods for inverse problems*, Inverse Problems, **22** (2006), R1–R47.
- [32] P. Martin, “Multiple Scattering: Interaction of Time-Harmonic Waves with N Obstacles,” Encyclopedia of Mathematics and its Applications, Cambridge University Press, 2006

Received September 2012; revised October 2012.

E-mail address: li.jz@sustc.edu.cn

E-mail address: hongyu.liuip@gmail.com

E-mail address: hpsun@amss.ac.cn

E-mail address: zou@math.cuhk.edu.hk